

Evaluation of SSMIS Upper Atmosphere Sounding Channels for High-Altitude Data Assimilation

KARL W. HOPPEL, STEPHEN D. ECKERMANN, LAWRENCE COY,* GERALD E. NEDOLUHA,
AND DOUGLAS R. ALLEN

Naval Research Laboratory, Washington, D.C.

STEVEN D. SWADLEY AND NANCY L. BAKER

Naval Research Laboratory, Monterey, California

(Manuscript received 21 December 2012, in final form 26 March 2013)

ABSTRACT

Upper atmosphere sounding (UAS) channels of the Special Sensor Microwave Imager/Sounder (SSMIS) were assimilated using a high-altitude version of the Navy Global Environmental Model (NAVGE M) in order to investigate their potential for operational forecasting from the surface to the mesopause. UAS radiances were assimilated into NAVGE M using the new Community Radiative Transfer Model (CRTM) that accounts for Zeeman line splitting by geomagnetic fields. UAS radiance data from April 2010 to March 2011 are shown to be in good agreement with coincident temperature measurements from the Sounding of the Atmosphere Using Broadband Emission Radiometry (SABER) instrument that were used to simulate UAS brightness temperatures. Four NAVGE M experiments were performed during July 2010 that assimilated (i) no mesospheric observations, (ii) UAS data only, (iii) SABER and Microwave Limb Sounder (MLS) mesospheric temperatures only, and (iv) SABER, MLS, and UAS data. Zonal mean temperatures and observation – forecast differences for the UAS-only and SABER+MLS experiments are similar throughout most of the mesosphere, and show large improvements over the experiment assimilating no mesospheric observations, proving that assimilation of UAS radiances can provide a reliable large-scale constraint throughout the mesosphere for operational, high-altitude analysis. This is confirmed by comparison of solar migrating tides and the quasi-two-day wave in the mesospheric analyses. The UAS-only experiment produces realistic tidal and two-day wave amplitudes in the summer mesosphere in agreement with the experiments assimilating MLS and SABER observations, whereas the experiment with no mesospheric observations produces excessively strong mesospheric winds and two-day wave amplitudes.

1. Introduction

The upper boundaries of NWP systems have been systematically increasing. Upward extension through the stratosphere was motivated initially by a need to assimilate radiances measured by operational meteorological satellite sensors. One example is the Special Sensor Microwave Imager/Sounder (SSMIS; Kunkee et al. 2008) on the operational satellites of the Defense Meteorological Satellite Program (DMSP). SSMIS scans the atmosphere

in a conical pattern distributed symmetrically about nadir. Vertical weighting functions (VWFs) for radiances acquired in a subset of the 24 SSMIS measurement channels are plotted in Fig. 1, and reveal that even nominal tropospheric channels (i.e., those with peak responses at tropospheric altitudes) have broad VWFs that extend deep into the stratosphere. Accurate assimilation of the atmospheric information contained in these radiances requires accurate background (forecast) fields of atmospheric parameters such as temperature and constituent concentrations that affect these channel radiances at all contributing altitudes. Thus, even to assimilate tropospheric and lower stratospheric radiance channels requires a forecast model extending to ~40–50-km altitude. In addition, Fig. 1 shows higher peaking SSMIS channels extending through the stratosphere and mesosphere, with tails extending to ~100-km altitude.

* Current affiliation: Science Systems and Applications, Inc., Lanham, Maryland.

Corresponding author address: Mr. Karl Hoppel, Naval Research Laboratory, Overlook Ave. S.W., Code 7227, Washington, DC 20375.
E-mail: karl.hoppel@nrl.navy.mil

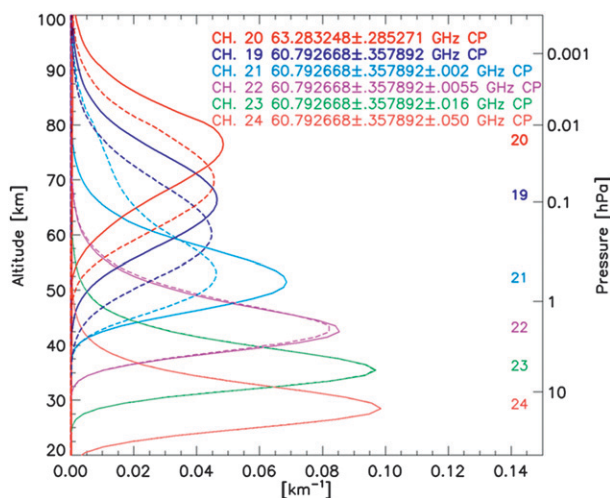


FIG. 1. SSMIS weighting functions for a weak geomagnetic field ($26 \mu\text{T}$) typical of equatorial regions (solid curves) and for a strong magnetic field ($60 \mu\text{T}$) typical of polar regions (dashed curves). Channels 19–21 are most sensitive to geomagnetic field changes through the Zeeman splitting of the O_2 microwave lines. The weighting functions are sensitive to both the field strength and orientation of the field with respect to the SSMIS viewing direction.

The objective of the current work is to assimilate the information contained in all SSMIS channels using a state-of-the-art prototype operational NWP system extending to ~ 100 -km altitude (i.e., to the “edge of space”). There are a number of reasons to extend operational NWP systems this high. First, it is now recognized that deep descending stratospheric circulation anomalies in polar winter can affect tropospheric weather prediction on time scales from weeks to months (e.g., Thompson et al. 2002; Baldwin et al. 2003; Charlton et al. 2004; Jung and Barkmeijer 2006; Ineson and Scaife 2009; Roff et al. 2011). Yet observations and modeling studies indicate that these circulation anomalies often form first in the mesosphere and lower thermosphere (MLT) up to a week before impacting the stratosphere (Dowdy et al. 2004; Coy et al. 2011), providing a potential for both advanced warning and improved predictability of these deep nonlinear dynamical features. Second, 0–100-km NWP systems are a necessary step toward integrated systems for ground-to-space weather prediction (e.g., Wang et al. 2011), an important initiative given emerging evidence that tropospheric and stratospheric meteorological disturbances have unexpectedly large impacts on space weather and its prediction (e.g., Goncharenko et al. 2010). Finally, there are emerging defense and civilian technologies that operate in the “near space” environment at altitudes ~ 20 –100 km and require forecast guidance for their operations.

The Naval Research Laboratory (NRL) developed an advanced-level physics, high-altitude (ALPHA) prototype

of the Navy Operational Global Atmospheric Prediction System (NOGAPS) that extended to ~ 100 km and assimilated observations, initially up to ~ 80 km (Hoppel et al. 2008) and later up to ~ 92 km (Eckermann et al. 2009). For these studies, mesospheric temperatures from two research satellite instruments were assimilated: the Sounding of the Atmosphere Using Broadband Emission Radiometry (SABER) limb sensor on the National Aeronautics and Space Administration (NASA) Thermosphere Ionosphere Mesosphere Energetics and Dynamics (TIMED) satellite, and the Microwave Limb Sounder (MLS) on board NASA’s Earth Observing System (EOS) *Aura* satellite. Since TIMED and *Aura* are research satellites, SABER and MLS observations are not generally available in near-real time, although some effort has been made recently to provide near-real-time MLS data products (Lambert et al. 2012).

Currently, SSMIS is the only operational meteorological sensor with upper atmospheric sounding (UAS) channels that provide measurements in the mesosphere (see Fig. 1). It is currently deployed on three separate DMSP satellites: *F16*, *F17*, and *F18*, with two additional instruments awaiting launch in the near future. The six UAS channels 19–24 use multiple, narrow spectral bands all located near line centers of the O_2 magnetic dipole transitions. The complicated microwave spectroscopy of these channels, resulting from the interaction of the O_2 absorption spectrum with the geomagnetic field leading to Zeeman splitting of the absorption lines, has hindered efforts to assimilate these observations. However, the required improvements to the fast forward radiative transfer (RT) modeling of the UAS O_2 bands are now available (Han et al. 2007). NWP forecast models having extended upper boundaries and new mesospheric physics packages offer the promise that the mesosphere might be accurately analyzed and forecast in an operational setting. However, it is unclear if UAS measurements have sufficient quality, geographical coverage, and vertical resolution to constrain the mesosphere accurately in an NWP system. In this study, we examine whether assimilation of SSMIS–UAS data in a high-altitude NWP system using fast RT modeling that includes the Zeeman splitting effect can provide realistic mesospheric analyses of comparable quality to those previously obtained from assimilating mesospheric temperature profiles from research satellites (Hoppel et al. 2008; Eckermann et al. 2009).

After describing the satellite data used in this study (section 2), we compare the UAS radiances with synthetic radiances derived from coincident limb temperature profiles from SABER (section 3). For this comparison we employ version 2 of the Community Radiative Transfer Model (CRTM) to convert the SABER temperature

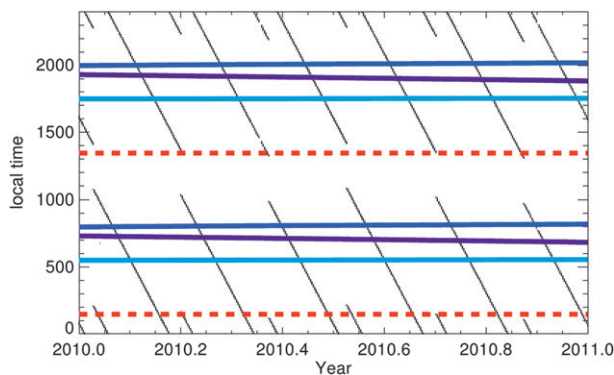


FIG. 2. Measurement local times (HHMM) at equatorial crossing during 2010 for SABER (thin black), MLS (red dashed), DMSP *F16* (purple), *F17* (light blue), and *F18* (dark blue).

profile into equivalent UAS brightness temperatures, illustrating the importance of correctly modeling the Zeeman effect. We then present results from four separate forecast-assimilation experiments using a preoperational high-altitude version of the Navy Global Environment Model (NAVGEN in section 4). We compare results from experiments that assimilated no mesospheric observations with those that assimilated mesospheric radiance and temperature observations from different combinations of instruments (SSMIS, SABER, and MLS). In addition to standard diagnostics, we also use mesospheric analysis fields from each NAVGEN experiment to study and compare amplitudes and dynamics of migrating solar tides and the quasi-two-day wave. We end with a summary and conclusions (section 5).

2. Satellite data description

a. SABER

SABER is a 10-channel broadband, limb-viewing, IR radiometer on the TIMED satellite. SABER obtains profiles from 52°S to 83°N for about 60 days in its “north viewing” mode, then switches (via a satellite yaw maneuver) to a “south viewing” mode (83°S–52°N) for the next 60 days, continuously repeating this sequence. Nearly continuous coverage is achieved equatorward of 52° latitude in each hemisphere (Remsberg et al. 2003). The vertical resolution of the retrievals is reported to be ~2 km, which is limited by the ~2-km vertical field of view of the instrument. For data assimilation, we treat SABER data as simple profiles because the vertical resolution is almost as good as the model resolution in the middle atmosphere (see section 4). Since TIMED is in a nonpolar 74.1° inclination orbit, the local time of the SABER measurements varies, so close space–time

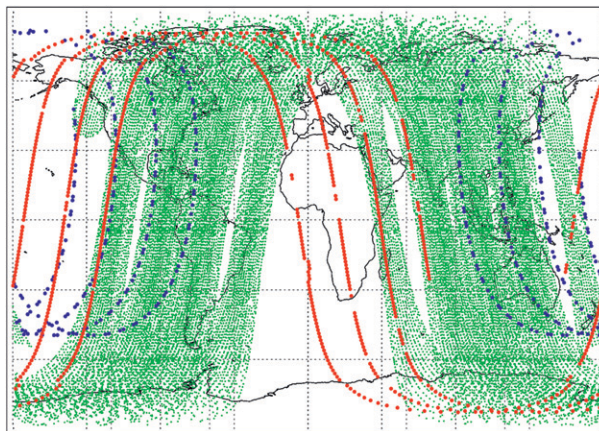


FIG. 3. Measurement locations for MLS (red), SABER (blue), and SSMIS on DMSP *F16*, *F17*, and *F18* (green) on 10 Jun 2010 for the 1200 UTC analysis.

coincidences can be found with all three of the SSMIS instruments, as illustrated in Fig. 2.

Stratospheric temperature is obtained from the 15- μ m radiation of CO₂. Here we use temperature profiles from the version 1.07 retrievals, which incorporate nonlocal thermodynamic equilibrium RT in the mesosphere as well as vibrational exchange between CO₂ isotopes (Kutepov et al. 2006; Garcia-Comas et al. 2008). Version 1.07 SABER temperatures were extensively studied and validated by Remsberg et al. (2008), who reported an estimated precision of ~1 K at 32 hPa (~25 km), monotonically increasing to ~4 K at 0.01 hPa (~80 km). Comparisons with independent observations and models indicated that version 1.07 SABER temperatures were too low by ~1 K in the upper stratosphere and by 2–3 K in the midmesosphere. In the thermosphere, the SABER temperature retrievals depend on composition data from the Whole Atmosphere Community Climate Model, which could be a source of systematic error.

b. Aura MLS

NASA's MLS (Waters et al. 2006) on the EOS *Aura* polar orbiter has been providing global temperature profiles since July 2004 that span the upper troposphere to lower thermosphere. By viewing the limb from the front of the *Aura* spacecraft, MLS continuously acquires data between 82°S and 82°N (see Fig. 3). The *Aura* orbit is sun synchronous and has a 1345 local equatorial crossing time (LT) on the ascending node (0145 LT descending). As shown in Fig. 2, these equatorial crossing times are ~4 h earlier than the closest SSMIS instrument, so there are no close time–space coincidences between MLS and SSMIS observations, except near the pole. MLS retrieves atmospheric temperature using limb observations of the 118-GHz O₂ and the 234-GHz O¹⁸O spectral

lines. We use the version 2.2 (v2.2) MLS temperatures described in Schwartz et al. (2008). The newer version 3.3 MLS temperatures are largely unchanged from v2.2 except in the troposphere (Livesey et al. 2011). The precision of the temperature measurement is 1 K or better at altitudes below 0.316 hPa (~ 55 km), but degrades to ~ 2.2 K at 0.01 hPa or ~ 80 km (Schwartz et al. 2008). Comparisons of MLS v2.2 temperatures with correlative datasets (Schwartz et al. 2008) showed that, while the bias in the stratosphere was generally less than 2 K when compared to other observations, there are some persistent vertical oscillations with respect to several other measurements near the stratopause, and these oscillations have amplitudes as large as 2–3 K. In the mesosphere MLS v2.2 temperatures are biased low (~ 0 –7 K) compared with a number of other correlative datasets.

The horizontal resolution of the MLS temperature measurements in the middle atmosphere is ~ 180 km along track and ~ 12 km cross track. The vertical resolution, expressed as the full-width half maximum of the averaging kernel, is ~ 3.5 km at 31.6 hPa, and degrades at altitudes above 20 hPa to ~ 6.2 km at 3.16 hPa and ~ 14 km at 0.01 hPa (Schwartz et al. 2008). Ideally, the broadening of the vertical weighting function in the mesosphere should be incorporated into the MLS assimilation, using a forward model to calculate a temperature Jacobian similar to radiance assimilation. Instead, we treat MLS here as a simple temperature profile, oversampled to the model vertical resolution, an approximation that may introduce some biases to the assimilation.

c. SSMIS

The SSMIS instruments measure Earth's radiation in 24 microwave channels using a conical scan cycle consisting of 180 measurements spanning 143.2° of azimuth at a constant off-nadir viewing angle of 45° , producing radiance imagery with a swath width of ~ 1700 km. The radiances are oversampled to ~ 12.5 km spacing between measurements (Kunkee et al. 2008). There are currently three SSMIS sensors in operation on the DMSP *F16*, *F17*, and *F18* satellites. These satellites are in sun-synchronous polar orbits with local equatorial crossing times that drift slowly in time (see Fig. 2). For measurements during 2010, the period focused on primarily in this study, the equatorial crossing times of ascending orbits are approximately 1820, 1737, and 2012 LT for *F16*, *F17*, and *F18*, respectively. The six UAS channels (numbers 19–24) measure the 60-GHz molecular oxygen absorption band, which is sensitive to temperatures in the upper stratosphere and mesosphere (see Fig. 1). The fast scanning pattern yields a greater geographical density of measurements than limb sensors like SABER and MLS, as illustrated in Fig. 3.

While all six UAS channels have been operational since about 2006, the three highest peaking Zeeman affected channels (numbers 19–21) have not, to our knowledge, been assimilated using an operational NWP system. The primary obstacles have been (i) the altitudes to which these channels are sensitive have exceeded the upper boundaries of many NWP systems, and (ii) the difficulty in accurately yet rapidly forward modeling radiances in SSMIS channels 19–21. The latter difficulty arises because the UAS channels use narrow spectral bands near the line centers of the O_2 magnetic dipole transitions. The Zeeman interaction of the O_2 molecule's electronic spin with Earth's magnetic field causes these lines to split (e.g., Stogryn 1989), producing partially polarized radiation and hence channel radiances that depend strongly on both the strength of the geomagnetic field as well as its orientation with respect to the incoming radiation. This Zeeman effect causes the shape and peak altitude of the weighting functions to vary by as much as ~ 10 km over each orbit and also as a function of scan angle (see Fig. 1), and must be taken into account using a fast RT model (described below). Another interesting feature is that the altitude of peak sensitivity in the VWFs for channels 19 and 21 move in opposite directions as the magnetic field changes. This creates a vertical sampling pattern that is often highly nonuniform and always a strong function of latitude. For more details about the UAS measurements, see Swadley et al. (2008). Although channels 22–24 are formally part of the UAS channels, they have insignificant Zeeman sensitivity and their weighting functions peak below ~ 1 hPa, overlapping with microwave radiances from other instruments. We will group these three channels with the “normal” SSMIS channels for our DA experiments and limit our evaluation to channels 19–21 in the remainder of this paper.

3. Comparisons of SABER-derived and SSMIS radiances

a. Radiative transfer calculations

Han et al. (2007, 2010) have developed a fast RT model for the SSMIS UAS channels that includes the Zeeman effect as well as the frequency shift due to Earth's rotation. By comparison with more accurate line-by-line spectroscopic calculations, Han et al. (2007) found that the fast RT model for channels 19, 20, and 21 had a root-mean-square error (rmse) of 0.34, 0.64, and 0.33 K, respectively. This RT calculation was recently added to the CRTM (version 2) developed by the NASA/National Oceanic and Atmospheric Administration (NOAA)/Air Force/Navy Joint Center for Satellite Data Assimilation. To make use of the SSMIS Zeeman capability, the

CRTM requires two new input parameters for each measurement: the geomagnetic field strength and the angle between the microwave antenna boresight and the geomagnetic field.

The UAS data for this work were processed and produced by the SSMIS-UAS Unified Preprocessor (UPP) that has been developed at NRL and patterned after the original UPP jointly developed by the Met Office and NRL (Bell et al. 2008). The UPP performs a two-dimensional Gaussian spatial averaging of the raw data in order to reduce the random channel noise. The estimated random errors for the observations, which are based on the noise equivalent delta temperature (NEDT) of the instrument channels (Swadley et al. 2010) and a spatial averaging Gaussian width of 75 km, are ~ 1.2 K for channels 19 and 20, and ~ 0.95 K for channel 21. The geolocation and the mean geocentric antenna boresight vector for each averaged observation are calculated at a height of 60 km. The geomagnetic field vector is taken from the International Geomagnetic Reference Field (IGRF) model (Macmillan and Maus 2005), also calculated at 60 km. The geomagnetic field in the mesosphere can be perturbed by space weather events, which are not represented by the IGRF model. We examined the time record of the Dst geomagnetic index (<http://wdc.kugi.kyoto-u.ac.jp/>), and found no large geomagnetic storms during the time periods used for the validations and experiments in this paper. Therefore, we leave the investigation of space weather effects on the UAS Zeeman calculations for future study.

b. Comparisons with SABER

Here we compare the SABER-derived brightness temperatures with SSMIS UAS radiances. This comparison is similar to that performed in Han et al. (2007), except that in addition to SSMIS *F16* data, here we have included data from *F17* and *F18*. To convert the SABER temperature profiles into radiances that would be observed by the UAS channels, the CRTM forward model requires temperature profiles down to the surface. Because SABER profiles do not reach the surface, we interpolate the NASA Goddard Earth Observing System version 5 (GEOS-5) analyzed temperatures (Rienecker et al. 2008) to the time and location of the SABER measurement and then splice the GEOS-5 and SABER temperature profiles together across an interface near 10 hPa. This provides a continuous temperature profile from the surface to 0.001 hPa. The CRTM forward model is then run using this merged temperature profile, together with the appropriate Zeeman parameters (magnetic field vector and antenna pointing vector) taken from the coincident SSMIS data. The output of the CRTM is a set of microwave brightness temperatures (Tb) simulated for each UAS channel.

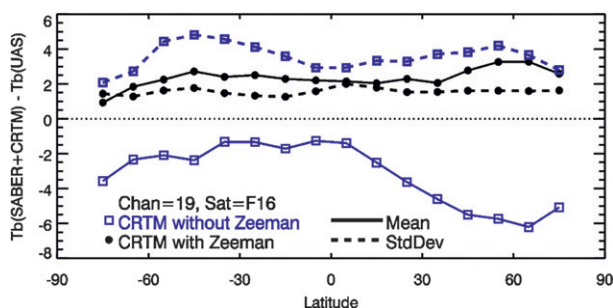


FIG. 4. Mean differences (solid curves) and standard deviations (dashed curves) between UAS channel 17 Tb and SABER/CRTM simulated Tb (K), and plotted as a function of latitude. Results are shown with (black) and without (blue) the CRTM Zeeman correction turned on; $\sim 35\,000$ coincident measurements from the 15th day of April 2010–March 2011 are included. See text for further details.

We choose data from the 15th day of each month from April 2010 to March 2011 in order to sample an entire year evenly. Despite using only one day of data per month, the total number of coincident profiles is greater than 30 000 for each SSMIS instrument. SABER and SSMIS measurements are considered to be coincident if they are made within 1° (~ 111 km great-circle distance) and 3 h of each other. SABER profiles are allowed to be coincident with multiple SSMIS soundings. The ± 3 -h time window was chosen to resolve tidal variations while providing coincidences over a large range of latitudes for almost every month.

To illustrate the importance of the Zeeman modeling, Fig. 4 shows coincident comparisons between SABER-derived and SSMIS brightness temperatures in channel 19 as a function of latitude, with and without inclusion of Zeeman splitting in the CRTM. Channel 19 is a nominal mesospheric temperature channel. When Zeeman splitting is included the mean Tb difference changes by 5 K or more, and reduces the variation with respect to latitude, most notably the large mean differences at high northern latitudes. The Zeeman correction also significantly reduces the standard deviation of the Tb differences. The largest reduction in standard deviation occurs in the southern midlatitudes where large geomagnetic variations as a function of longitude due to the South Atlantic anomaly (Macmillan and Maus 2005) give rise to enhanced variance in raw (Zeeman uncorrected) Tb measurements as a function of longitude.

The coincidence results are summarized in Fig. 5, which includes zonal-mean biases and standard deviations for channels 19, 20, and 21 from each of the three SSMIS instruments, averaged in 10° latitude bins. In each panel the results are separated into ascending, descending, and all-orbit segments, to delineate any local time dependence (such as day–night asymmetries) or unexplained

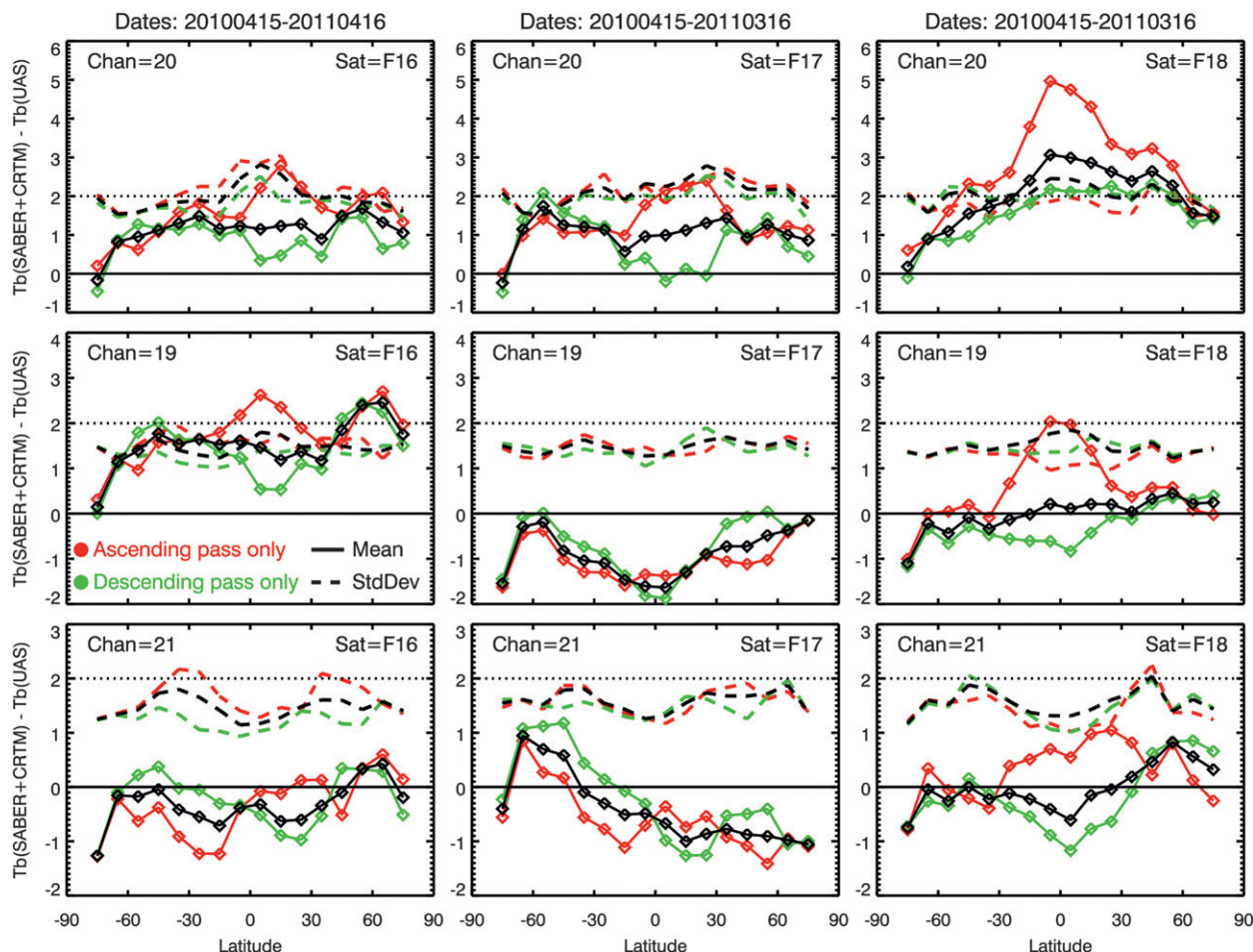


FIG. 5. Means (solid curves) and standard deviations (dashed curves) vs latitude of differences between forward-modeled SABER temperatures and SSMIS brightness temperatures on (left) *F16*, (middle) *F17*, and (right) *F18* for SSMIS channels (top) 20, (middle) 19, and (bottom) 21. Red, green, and black curves show results for ascending, descending, and all-orbital segments, respectively.

instrument effects. The standard deviations of the T_b differences are ~ 1.5 – 2 K, which is slightly larger than the estimated random UAS errors given in section 2c. The standard deviations are quite small considering uncertainties associated with systematic errors in SABER (see section 2a), errors in the CRTM, and the imperfect coincidences. The component of the biases that appears as a global-mean offset can easily be removed during data assimilation by modern radiance bias correction schemes used in NWP (e.g., Harris and Kelly 2001; Dee and Uppala 2009). The comparisons reveal meridional structure with an amplitude of ~ 2 K. Although there are some large ascending/descending orbit differences, the ascending and descending coincidences tend to cluster at different local times and seasons, so the differences are difficult to interpret. If the meridional structure reflects biases in the UAS data (as opposed to errors in CRTM modeling, SABER, or imperfect coincidences), then

removing it using a bias correction scheme could be difficult. If a bias correction scheme allows latitude-dependent corrections, it also has the capability to reinforce latitude-dependent model biases. Forecast model biases are expected to be larger in the mesosphere than troposphere because the mesospheric physics are not as well developed. Chemical heating is not included (this is important above ~ 0.01 hPa), the gravity wave drag is not yet tuned optimally, and the current parameterizations of radiative heating and cooling rates are not designed to operate accurately at altitudes above ~ 70 km. The resulting temperature biases are expected to vary in latitude between the winter hemisphere, tropics, and summer hemisphere, with larger random error due to difficulties representing temperature variability at small scales (e.g., Nezlin et al. 2009). Nevertheless, UAS data with uncorrected, ~ 2 -K errors can be expected to still have a positive impact on mesospheric temperature analyses when model errors are larger.

Performing a similar coincident comparison with MLS observations is problematic. First, as noted in section 2b, close MLS–SSMIS coincidences only occur near the poles. Second, the MLS weighting functions are vertically broad in the mesosphere (Schwartz et al. 2008). The CRTM assumes that the resolution of the input atmospheric profiles matches that of the internal model grid, but MLS temperatures smooth out the true temperature structure such as the minimum at the mesopause. Also, there are unexplained systematic differences between MLS and SABER polar temperatures that need to be understood before differences between UAS–MLS and UAS–SABER comparisons can be interpreted.

4. Assimilation tests

a. Assimilation system description

For testing the assimilation of UAS channel radiances, we use a modified *preoperational* version of the Navy's new operational NWP system: NAVGEM. This system uses the four-dimensional variational data assimilation (4D-Var) algorithm described in Xu et al. (2005) and Rosmond and Xu (2006). The forecast model uses a new semi-Lagrangian (SL) dynamical core that includes many of the physics packages from the previous operational Eulerian forecast model in NOGAPS, but also includes new physics and features. NAVGEM replaced NOGAPS as the Navy's operational NWP system in 2013 with a T359L50 configuration extending to 0.04 hPa. For our experiments, the number of vertical levels in the SL model was increased from 50 to 60 with a top at 0.005 hPa and a vertical resolution of ~ 2 km throughout the stratosphere and mesosphere (see Fig. 1 of Eckermann 2009). The horizontal resolution was reduced from T359 to T239 (0.75° resolution).

To assimilate the UAS radiances, the SL model must have a reasonable representation of the mesosphere, so that innovations (observations minus NWP model background, or O-Fs) and analysis corrections are not too large. We therefore made two important modifications to the model physics. The previous NOGAPS radiation codes have recently been replaced in NAVGEM in favor of the Rapid Radiative Transfer Model for GCMs (RRTMG; Mlawer et al. 1997; Iacono et al. 2000; Clough et al. 2005), which contains more bands and is accurate up to higher altitudes of ~ 0.1 hPa. The scheme gives results above this level but errors grow because of nonlocal thermodynamic equilibrium effects and missing shortwave heating terms. As discussed in section 3 of Eckermann et al. (2009), carefully tuned parameterizations of subgrid-scale gravity wave drag are critical to achieving reasonable mesospheric forecast temperatures and minimizing

assimilation bias. Here we implement a single-wave stochastic analog of the 65-wave nonorographic gravity wave drag parameterization of Garcia et al. (2007), as described by Eckermann (2011). Tuning of the gravity wave parameterization was performed using the January 2009 time period and minimizing the temperature differences between 5-day forecasts and MLS measurements.

Despite these additions, the NAVGEM SL model physics and validation are still in their beginning stages of development at these altitudes, so that the mesosphere and lower thermosphere are less accurately simulated than in models designed specifically to focus on middle atmosphere assimilation, such as the NOGAPS-ALPHA 3D-Var high-altitude assimilation system (Eckermann et al. 2009) and the Canadian Middle Atmosphere Model Data Assimilation System (Ren et al. 2011). Since assimilated observations are a critical prerequisite for objectively diagnosing and then eliminating model bias, we consider the current NAVGEM study as one of the preliminary, essential first steps of a long-term effort to extend operational NWP through the mesosphere.

Our assimilation experiments use a radiance bias correction scheme that follows the methodology of Harris and Kelly (2001). There are four bias predictors (or regression terms) used for radiances: a constant term, conical scan angle, and geopotential thickness of the 300–850- and 50–200-hPa layers. The SSMIS bias estimation includes an additional ascending/descending pass predictor. For simplicity, the same bias correction scheme is applied to all radiance data, including the UAS radiances. SABER and MLS data are not subject to an automatic bias correction scheme. However, a global pressure-dependent static temperature correction is applied to the MLS temperatures. This correction is a vertically smoothed version of the MLS–SABER differences found in the MLS validation study of Schwartz et al. (2008). From 1.5 to 0.7 hPa, the estimated MLS bias is positive with a peak value of +5 K at 1 hPa. The bias is negative at higher altitudes, increasing from -1 K at 0.46 hPa to -3.8 K near the model top at 0.005 hPa.

We performed four data assimilation experiments. All experiments assimilated the Navy's standard operational set of observations including conventional observations (e.g., radiosondes), GPS radio occultation bending angles, microwave radiances from SSMIS and the Advanced Microwave Sounding Unit-A (AMSU-A), and IR radiances from the Infrared Atmospheric Sounding Interferometer (IASI) and the Atmospheric Infrared Sounder (AIRS). These standard radiance data all have weighting functions that peak below about 1 hPa and include the three lower peaking UAS channels (22–24). Each of the four experiments assimilated a different combination of mesospheric measurements. In the first

experiment, labeled “MLS+SABER,” we assimilated MLS and SABER temperature profiles that cover the stratosphere and mesosphere. The second experiment, labeled “UAS,” assimilated the three SSMIS-UAS high-peaking channels 19–21, but did not assimilate either MLS or SABER data. The third experiment, labeled “MLS+SABER+UAS,” assimilated SSMIS-UAS radiances, and SABER and MLS temperatures. Although some of the MLS and SABER observations are in the stratosphere, we expect the analysis below the 1-hPa level to be dominated by the standard data and show only small differences below that level. These three analysis experiments were spun up during the last two weeks of June and continued through to the end of July 2010. A fourth experiment that did not assimilate any mesospheric observations was performed to quantify the importance of assimilating mesospheric observations. This experiment, labeled “NoMesoObs,” covers only the 1–15 July time period, which was sufficiently long for the analyzed mesospheric state to diverge rapidly from that of the other three experiments, as demonstrated explicitly below. An example of the spatial sampling of the SSMIS-UAS, SABER, and MLS observations for a single 6-h analysis window is shown in Fig. 3.

b. Zonal mean and O-F temperature comparisons

The zonal-mean temperature analyses for 14 July 2010 at 1200 UTC are shown in Fig. 6 for the MLS+SABER, UAS, and NoMesoObs experiments. Although the MLS and SABER observations are sparse (see Fig. 3), the MLS+SABER assimilation produces a zonal-mean temperature that is very similar to the temperature distribution obtained from directly averaging the MLS and SABER observations (not shown). Furthermore, previous NOGAPS-ALPHA experiments assimilating MLS and SABER temperatures produced mesospheric temperature analyses that agreed closely with independent mesospheric temperature observations (see, e.g., Fig. 5 of Eckermann et al. 2009). Therefore, we take Fig. 6a to represent our best estimate of the truth with regard to the zonal-mean temperature, revealing as it does realistic cold polar summer (northern) mesospheric temperatures and a realistic separated winter (southern) polar stratopause structure. Zonal-mean temperatures from the UAS assimilation experiment in Fig. 6b have a similar distribution, but some differences with the MLS+SABER results are apparent, most notably in the high-latitude Southern Hemisphere. The UAS assimilation is also a little colder near the model top (~ 5 K colder at 0.01 hPa).

However, temperatures from the NoMesoObs experiment in Fig. 6c show much larger and more significant temperature differences in the mesosphere, and even near the stratopause (identified by the temperature

maximum), relative to the other two experiments. The southern (winter) stratopause is higher, the equatorial upper mesosphere is colder, and the northern (summer) mesopause is warmer. These temperature differences, along with differences in the zonal wind (see discussion of Fig. 10) suggest that the model parameterized gravity wave drag is too weak in the mesosphere. Assimilating only UAS radiances in the mesosphere is a large improvement over the experiment that assimilated no mesospheric observations. Figures 6b,c also directly demonstrate how UAS radiance assimilation can be used to improve model physics in the mesosphere to eliminate model bias, given that radiative heating and cooling parameterizations act directly on temperature, while, as demonstrated in section 3 of Eckermann et al. (2009), mesospheric gravity wave drag tuning in forecast models also focuses primarily on eliminating zonal-mean temperature biases.

There is always a concern that our use of an updating radiance bias correction scheme in these experiments might reinforce model bias by falsely diagnosing model bias as radiance bias. This is especially true if the bias predictors (i.e., constant value, scan angle, layer thicknesses, etc.) correlate with the model bias. The two geopotential predictors that were used can only fit a very broad equator-to-pole variation. The SABER and MLS data in the MLS+SABER+UAS experiment provide an absolute reference, or anchor, for the UAS bias calculation that is absent in the UAS-only experiment. In comparing the computed UAS biases for these two experiments, we find that for channels 19 and 21 of each instrument, the mean biases differ by less than ~ 0.5 K between experiments. The computed biases also showed no significant time variations over the 1-month analysis. For channel 20, the UAS+SABER+MLS experiment generates mean biases that are ~ 1.5 – 2 K colder than the UAS-only experiment. This is consistent (as in Fig. 6) with the SABER+MLS+UAS analysis being warmer on average at 0.01 hPa by ~ 5 K relative to UAS-only analysis, and may indicate that the UAS-only correction is influenced by model bias. Also, because the model top is at ~ 0.005 hPa, and channel 20 is sensitive to levels above 0.001 hPa (see Fig. 1), there will be UAS forward modeling errors that are not represented in the SABER–UAS comparisons. We experimented with the CRTM model and found that the modeled channel 20 Tb increased by ~ 2 K when using a temperature profile that is truncated at 0.005 hPa. Therefore, it is difficult to interpret the bias corrections from the analysis experiments relative to the previous SABER–UAS comparisons. In the future, it may be preferable to apply a static UAS bias correction based on the MLS+SABER data and exclude any geophysical predictors until model biases are sufficiently diagnosed and corrected.

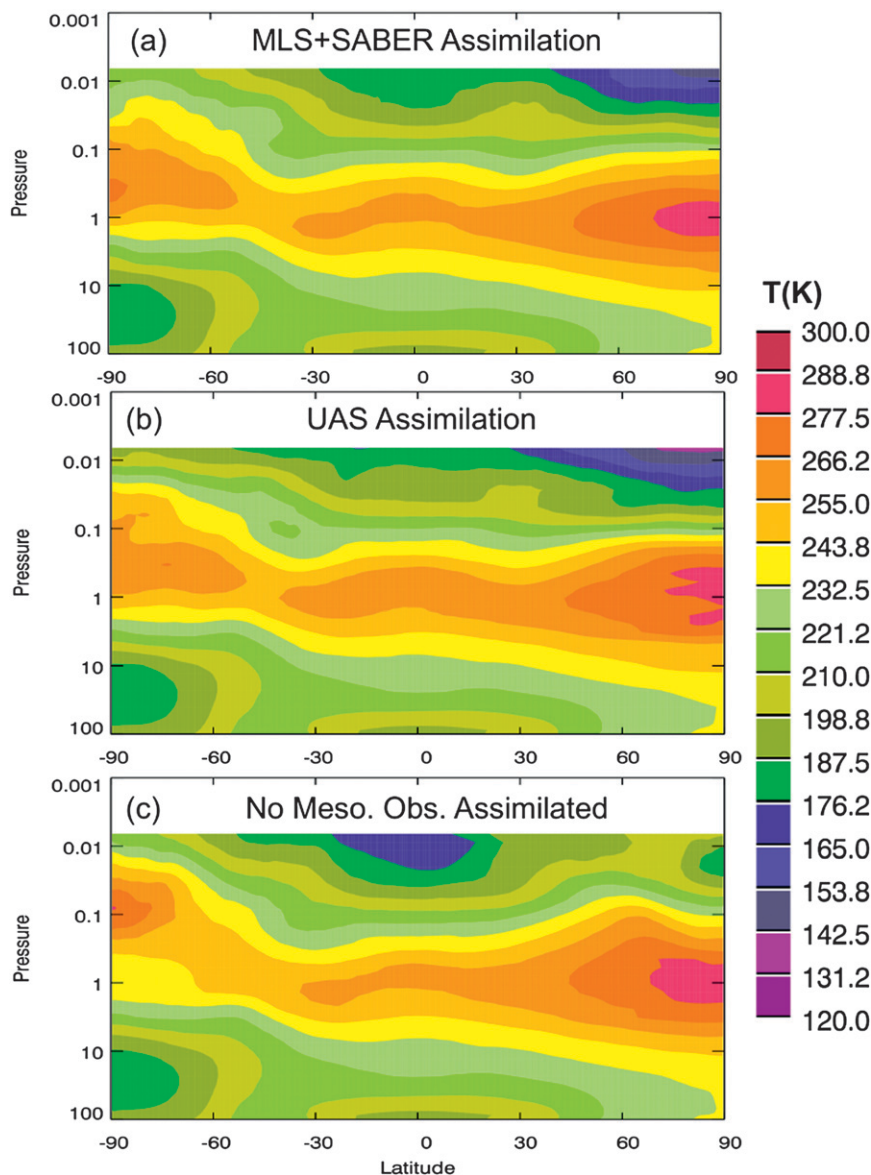


FIG. 6. Zonal mean temperature (see color bar on right for contour levels and units) from pole to pole (90°S – 90°N) and from ~ 100 to 0.01 hPa (~ 16 – 80 -km altitude) at 1200 UTC 14 Jul 2010 from experiments (a) MLS+SABER, (b) UAS, and (c) NoMesoObs. See text for further details.

Next, we examine the differences between the observations and the background forecast, or O-Fs, for these experiments. The O-Fs are calculated as part of the analysis and are essentially the forecast interpolated to the observation locations, with the additional application of the observation operator for radiance data. Because the background forecast is sampled over a very short interval (3–9 h) relative to the previous analysis state, the O-Fs can be interpreted as being an approximate measure of the error in the analysis. They include residual model biases that are not fully corrected by the

observations, and forecast errors arising from weather features and scales of variability that are not sufficiently constrained by the assimilation of observations. For each run, the standard deviation of the O-Fs was calculated for all observations, even for the observations that were not assimilated as part of the experiment (i.e., not used in that experiment's 4D-Var solution). In this way, for example, we can evaluate the MLS O-Fs even for the experiments that did not assimilate MLS data. Figures 7a–c show the MLS, SABER, and UAS-F18 O-F standard deviations, respectively, averaged from 5 to 31

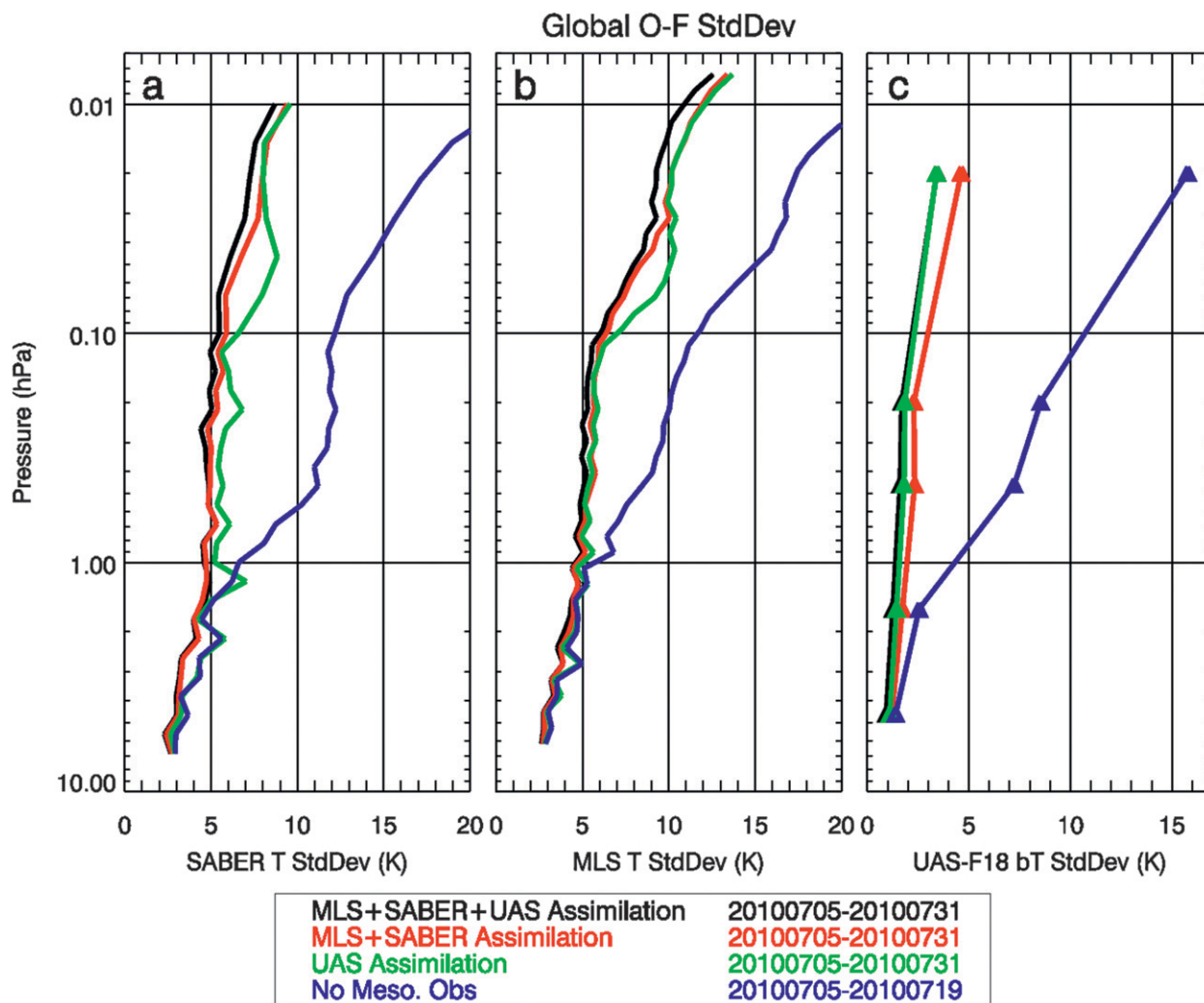


FIG. 7. Standard deviation (K) of the global O-F for (a) MLS temperature, (b) SABER temperature, and (c) *F18* UAS brightness temperature, averaged over the period 5–31 Jul 2010 for experiments MLS+SABER+UAS (black), MLS+SABER (red), and UAS (green). Results from the NoMesoObs experiment (blue) were averaged over the period 5–19 Jul 2010.

July 2010. Each panel plots four separate curves corresponding to results from each of the four NAVGEM experiments. The plots reveal very large O-F standard deviations for the NoMesoObs analysis above the 1-hPa level. Not only are the NoMesoObs standard deviations large, but the mean O-Fs are also large, as suggested by comparing Figs. 6a,b with Fig. 6c. The second important point is that assimilating only UAS data reduces the SABER and MLS O-Fs to levels nearly as small as when only MLS and SABER observations are assimilated. A third point is that assimilating all the observations in the MLS+SABER+UAS experiment yields the smallest SABER and MLS O-F standard deviations, but only slightly smaller than for the MLS+SABER experiment. Reduction in SABER and MLS O-F standard deviations is limited ultimately by the observation random error,

geographically varying biases between model and observations, biases among MLS, SABER, and UAS data, and fundamental predictability limits at smaller scales in the mesosphere. In Fig. 7c the O-F standard deviations for the *F18* UAS brightness temperatures T_b are plotted at the approximate mean pressure levels of the weighting function peaks. The overall results are similar to the MLS and SABER O-F comparisons, with the expected feature that assimilating UAS data reduces the O-F relative to MLS+SABER.

c. Examination of analyzed planetary-wave structures in the mesosphere

To assess the UAS mesospheric analyses further, we next study the amplitudes of three major planetary wave modes that are episodically energetic at these altitudes.

Solar forced tidal motions are a major component of mesospheric meteorology at all latitudes and seasons. For simplicity, we focus solely on the solar migrating diurnal and semidiurnal tides [westward-propagating diurnal wavenumber 1 (DW1) and semidiurnal wavenumber 2 (SW2)], leaving analysis of the potentially rich spectrum of nonmigrating tidal modes for future work. We also study the quasi-two-day wave [westward-propagating wavenumber 3 (Q2DW3)], which often attains large amplitudes in the extratropical summer mesosphere at the solstices.

At each gridded latitude and pressure for the period 1–14 July 2010, the analyses from each experiment provide a two-dimensional array of temperatures as a function of longitude and time, to which we applied a two-dimensional (longitude–time) fast Fourier transform (FFT). The resulting complex Fourier coefficients, containing both amplitude and phase information, were combined to yield a peak amplitude estimate averaged within spectral regions corresponding to the DW1 (westward wave 1, 0.93–1.08 days), SW2 (westward wave 2, 0.5–0.56 days), and Q2DW3 (westward wave 3, 1.56–2.80 days). By applying this FFT algorithm at every latitude and pressure, we compile estimates of the peak temperature amplitudes of these three planetary-wave modes, averaged over the 1–14 July 2010 period, as a function of latitude and height (pressure). In Fig. 8, these peak planetary-wave amplitudes as a function of latitude at 0.02 hPa (~ 76 km) are plotted, while in Fig. 9 vertical profiles of these amplitudes at selected latitudes are plotted.

We begin by comparing mesospheric tidal temperature amplitudes from each experiment to independent observational estimates. Truly independent observational validation is difficult in the mesosphere since available observations are sparse; SABER temperatures have proven to be the most important source of tidal temperature information to date. Since TIMED's nonpolar orbit (see section 2a) yields a SABER sampling pattern that precesses slowly through local time (~ 12 min day^{-1} ; see black curves in Fig. 2), mean tidal amplitudes can be estimated directly from the SABER temperature record with reasonable accuracy at a time resolution of approximately 1 month (provided certain geophysical stationarity assumptions hold; Meek et al. 2011). By analyzing SABER temperatures in this way from 2002–07, Mukhtarov et al. (2009) found local maxima in DW1 temperature amplitudes at ~ 75 – 80 km in July of ~ 8 K near 10°S and ~ 3 – 4 K near 35°S (see their Figs. 1 and 9b), in good agreement with the results of all of our NAVGEM experiments in Fig. 8a. Similar DW1 peak values and latitudes in July were also reported by Huang et al. (2010) based on their study of the 2004 SABER

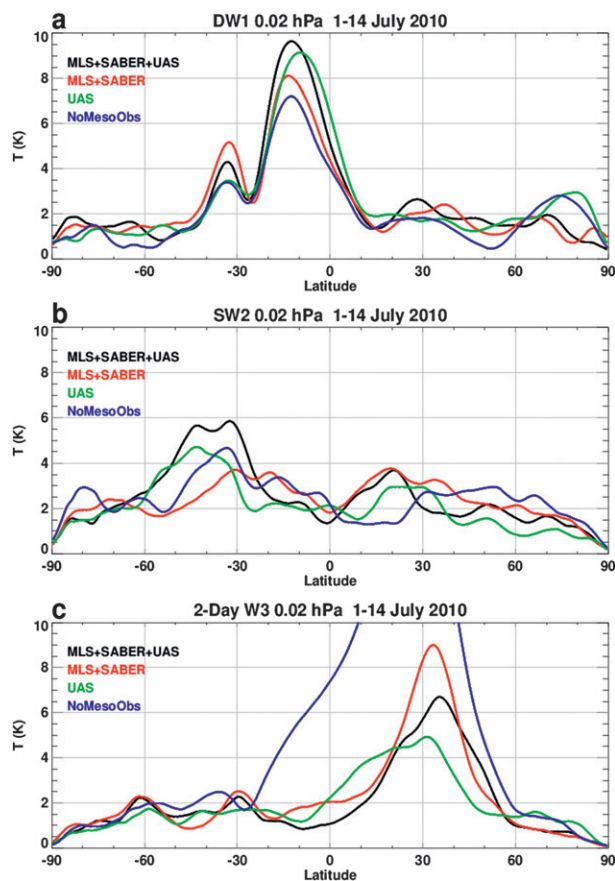


FIG. 8. Peak temperature amplitude (K) at 0.02 hPa (~ 76 km) as a function of latitude over the period 1–14 Jul 2010 for (a) DW1 (diurnal migrating tide), (b) SW2 (semidiurnal migrating tide), and (c) Q2DW3 (quasi-two-day wave), for assimilation experiments MLS+SABER+UAS (black), MLS+SABER (red), UAS (green), and NoMesoObs (blue).

temperature record (see their Fig. 6d). Likewise, the NAVGEM SW2 amplitudes in Fig. 8b are in reasonable agreement with monthly SABER SW2 estimates of Zhang et al. (2006) and Pancheva et al. (2009), although the uncertainties in estimating SW2 directly from the sparsely sampled SABER data used in these studies appear to be greater than for DW1 (Manson et al. 2010; Meek et al. 2011).

A striking result in Figs. 8a,b, as well as for the profiles in Figs. 9a,b, is that the NoMesoObs experiment, which assimilated no mesospheric observations at all, produces tidal amplitudes that are similar to those from the other three experiments assimilating various subsets of the MLS, SABER, and SSMIS mesospheric observations. The NoMesoObs experiment is similar in many ways to the standard configurations of other prototype NWP systems that have extended upper model boundaries through the mesosphere yet continue to assimilate only

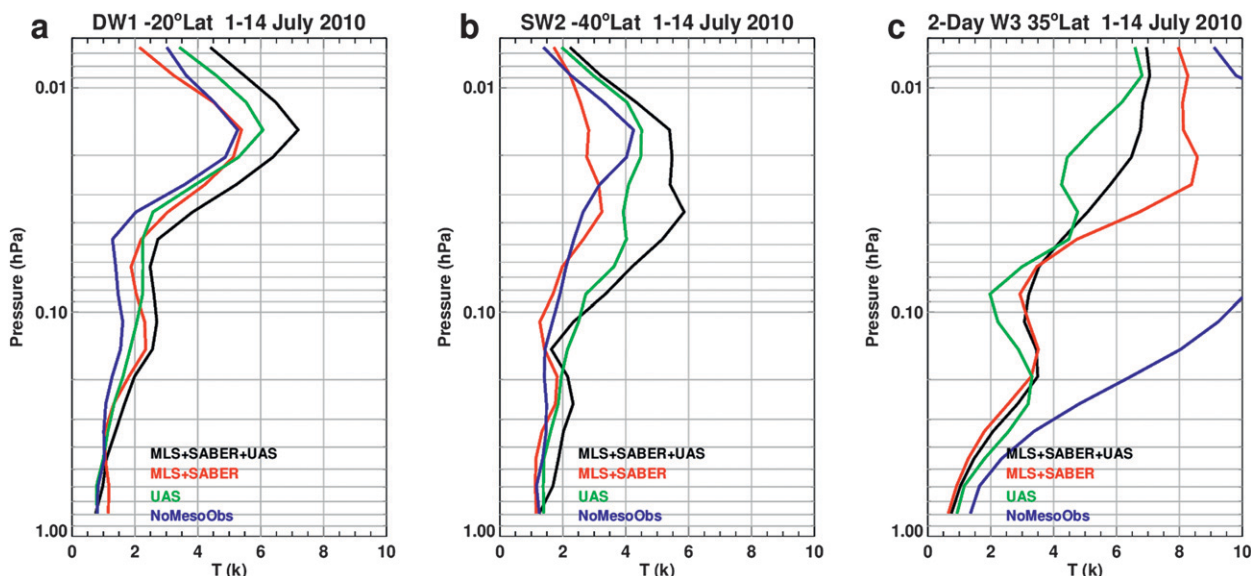


FIG. 9. Peak temperature amplitude (K) as a function of pressure from ~ 1 to 0.01 hPa during 1–14 Jul 2010 for (a) DW1 at 20°S , (b) SW2 at 40°S , and (c) Q2DW3 at 35°N , for the assimilation experiments MLS+SABER+UAS (black), MLS+SABER (red), UAS (green), and NoMesoObs (blue).

operationally available observations from the troposphere and lower-middle stratosphere (Polavarapu et al. 2005; Wang et al. 2011). If care is taken to minimize the filtering of tidal structures in the data assimilation algorithm (Sankey et al. 2007), the forecast models in these systems consistently reproduce reasonable mesospheric migrating tidal structures despite the absence of any local mesospheric data assimilation constraint (Sankey et al. 2007; Xu et al. 2011, 2012; Wang et al. 2011), consistent with the findings here.

This can be understood to first order by noting that migrating tides are generated by diabatic processes in the lower atmosphere that are well modeled by modern forecast models and tightly constrained by the assimilation of dense global observations of temperature, moisture, and ozone, giving rise to reasonably accurate forecasts and analyses of migrating tides throughout the troposphere and stratosphere (see, e.g., Sakazaki et al. 2012). The fast horizontal phase velocities of the forced migrating tidal modes mean that they subsequently propagate rapidly into the mesosphere, interacting minimally with the comparatively slower background mesospheric winds at these levels compared to other slower planetary- and gravity wave modes. Thus, inaccuracies in the forecast mesospheric state have limited first-order impact on tidal propagation into the mesosphere. Nonetheless, local mesospheric dynamical processes are known to affect mesospheric tidal amplitudes through various mechanisms, such as local advection and refraction, planetary wave-wave interactions, and gravity wave drag

(e.g., McLandress 2002; Riggin et al. 2003; Watanabe and Miyahara 2009; McCormack et al. 2010), which may explain some of the differences also evident among the experiments in Fig. 8. For example, DW1 amplitudes in the NoMesoObs experiments in Figs. 8 and 9 are systematically lower than in the other three experiments that assimilated mesospheric observations.

By contrast, much larger differences between the NoMesoObs experiment and the other three experiments emerge for the Q2DW3 amplitude in Figs. 8c and 9c. In particular, the Q2DW amplitude for the NoMesoObs experiment peaks off scale at $\sim 18\text{ K}$ in Fig. 9c, and is everywhere clearly and systematically much larger than in the other three experiments that assimilated mesospheric observations. Gray contours in Fig. 10 show the zonal mean zonal wind \bar{u} averaged over 1–14 July 2010 from each experiment. The three experiments assimilating mesospheric observations (Figs. 10a–c) all show a summertime easterly jet peaking at speeds $\sim 100\text{ m s}^{-1}$ with broadly similar (and realistic) latitude–height structure. By contrast, extratropical winds from the NoMesoObs experiment in Fig. 10d are substantially different, with the easterly jet being unrealistically strong and not “closed,” but instead increasing continuously with height right through the mesosphere—a clear indication of excessively weak parameterized nonorographic gravity wave drag in the forecast model. Overlaid green filled contours in Fig. 10 show the corresponding peak Q2DW3 temperature amplitudes. In all four experiments, these amplitudes peak on the equatorward flank of the westerly

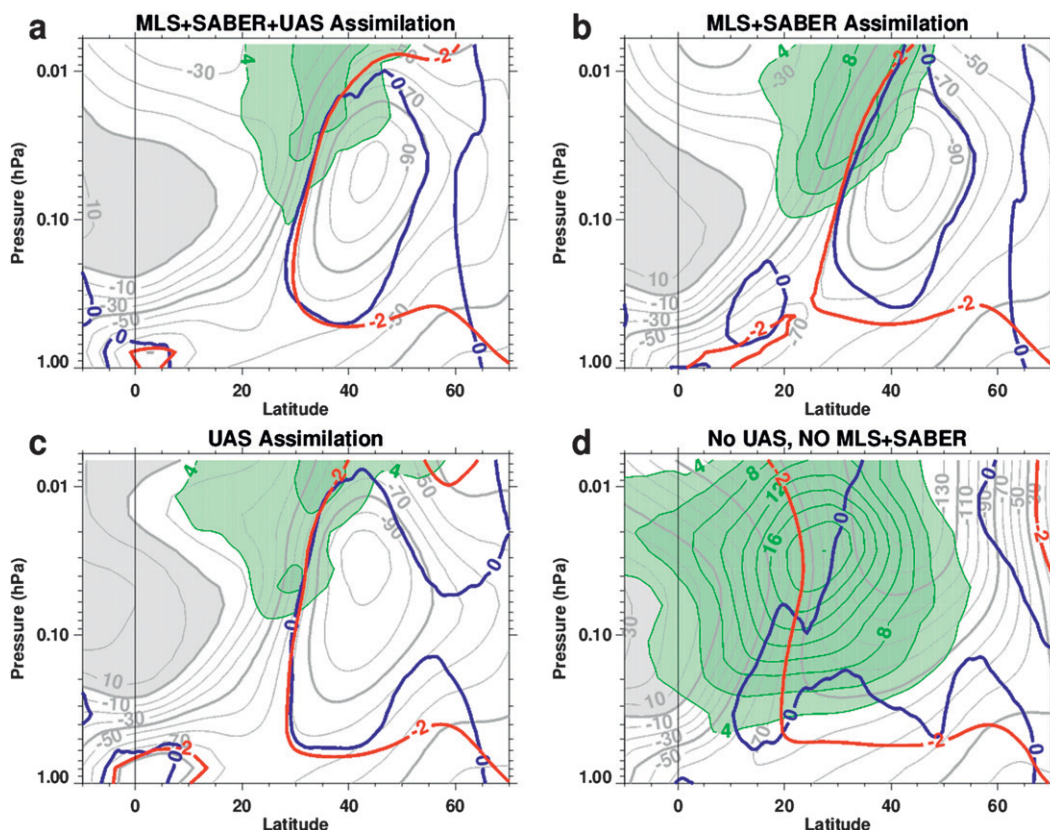


FIG. 10. Latitude–pressure cross sections during 1–14 Jul 2010 of the zonal mean zonal wind [gray contours, 10 ms^{-1} contour interval, positive (eastward) values are gray shaded], Q2DW3 temperature amplitudes (green contours and shading, contour interval 2 K, lowest contour shown 4 K), zero contour of meridional gradient of the quasigeostrophic potential vorticity (blue curve), and two-day wavenumber 3 critical line (red curve), for experiments (a) MLS+SABER+UAS, (b) MLS+SABER, (c) UAS, and (d) NoMesoObs.

mesospheric jet core, but the activity is larger and distributed over a much broader spatial area in the NoMesoObs experiment (Fig. 10d) relative to the other three experiments that assimilated mesospheric observations.

The close associations in Fig. 10 between peak Q2DW3 amplitudes and mesospheric jet structure are consistent with our understanding of mesospheric Q2DW3 dynamics, which develop locally as a forced planetary-scale quasi-normal-mode response to baroclinic instability of the easterly summertime mesospheric jets (Plumb 1983). To quantify this in each experiment, we computed the meridional gradient of zonal-mean potential vorticity \bar{q}_φ as [Eq. (5.3.4) of Andrews et al. (1987)]

$$\bar{q}_\varphi = 2\Omega \cos\varphi - \left[\frac{(\bar{u} \cos\varphi)_\varphi}{a \cos\varphi} \right]_\varphi - \frac{a}{\rho_0} (\rho_0 \varepsilon \bar{u}_z)_z, \quad (1)$$

where φ is latitude; z is pressure height (log-pressure coordinate); Ω is Earth's angular frequency; a is Earth's radius; ρ_0 is the basic state (zonal mean) density;

$\varepsilon = f^2/\bar{N}^2$, where f is the Coriolis parameter and N is buoyancy frequency; and overbars denote a zonal average. For these calculations, \bar{N}^2 , the zonal-mean static stability, was taken to be constant of $4 \times 10^{-4} \text{ s}^{-2}$, while zonal-mean density ρ_0 was taken to vary vertically with a constant density scale height of 7 km, whereupon \bar{q}_φ in (1) depends only on the gradients in \bar{u} . Blue curves in Fig. 10 plot $\bar{q}_\varphi = 0$ contours, which identify local zones in each experiment's mesospheric analysis that satisfy the necessary condition for baroclinic instability (Charney and Stern 1962). In the mesospheres of all four experiments, the location and latitude–height tilting of these $\bar{q}_\varphi = 0$ contours correspond closely with the location and tilt of the peak Q2DW3 amplitudes, consistent with local Q2DW3 generation from baroclinically unstable mesospheric shear zones in each experiment. Furthermore, red contours plot theoretical critical lines for a linear Rossby mode of wavenumber 3 and a period of 2 days. These generally coincide closely in Fig. 10 with the $\bar{q}_\varphi = 0$ contours in the active Q2DW3 regions, which, according to linear instability theory, is required for

a strong Q2DW3 response to the local baroclinic instability (Plumb 1983). While the red and blue curves are almost coincident within the Q2DW3 peak regions in Figs. 10a–c, they diverge more for the NoMesoObs experiment in Fig. 10d, suggesting in this case that nonlinear effects may be important, possibly yielding more broadband wave responses over wider wavenumber and period bands.

The large differences in Q2DW3 amplitudes between the NoMesoObs experiment and the other three are entirely consistent with the correspondingly large differences in \bar{u} and \bar{q}_ϕ . In particular, a number of previous modeling studies have shown that Q2DW3 generation and amplitudes are very sensitive to the parameterized gravity wave drag controlling the structure of the mesospheric summertime jet (e.g., Norton and Thuburn 1999), and the NoMesoObs wind structures are clearly unrealistic because of insufficient parameterized gravity wave drag. Some of the smaller differences in Q2DW3 amplitude among the three experiments assimilating mesospheric observations could also originate from wind differences due to broader UAS nadir weighting functions that underestimate local temperature (and hence wind) gradients controlling the structure of these baroclinic shear zones. Nonetheless, the results in Figs. 10c,d highlight again the value of the assimilated UAS observations in identifying and correcting large forecast model biases in the mesosphere, yielding corrected analysis fields of comparable quality to those using MLS and SABER data. For operational NWP, these UAS data provide objective measurements that quantitatively diagnose these mesospheric forecast biases, which can in turn drive targeted improvements to the forecast model's mesospheric parameterizations, such as retuned nonorographic gravity wave drag controlling winds and baroclinic instability relevant to the generation of Q2DW3. The progressive reduction in model bias made possible by the UAS assimilation should improve both the operational mesospheric assimilations and the forecast skill at these upper altitudes (Dee and daSilva 1998), making mesospheric prediction with operational NWP systems potentially feasible.

5. Summary and conclusions

SSMIS is continuously acquiring atmospheric radiances from the operational DMSP *F16*, *F17*, and *F18* polar orbiters, yet to date observations from its three highest peaking UAS channels, spanning altitudes ~40–100 km, have not been fully utilized by any operational NWP system. The study has focused on redressing this gap by (i) carefully comparing the UAS radiances to forward-modeled research quality stratospheric and mesospheric

temperatures acquired by SABER, (ii) developing a high-altitude NWP configuration capable of providing forecast backgrounds over the height range of the UAS measurements, and (iii) implementing the latest (version 2) CRTM incorporating the Zeeman splitting of UAS microwave lines by geomagnetic fields. Task (i) revealed that, sampled over a year of selective coincident observations, the UAS brightness temperatures agreed closely with synthetic UAS brightness temperatures obtained by forward modeling SABER temperature profiles using the CRTM, but only when Zeeman effects were included in the CRTM calculations. The standard deviations of the temperature differences were ~1.5–2 K. The biases were generally below 4 K, and were dominated by a global mean offset and large-scale meridional variations, both of which can be mitigated by an appropriately tuned bias correction scheme in a NWP assimilation.

Tasks (ii) and (iii) led to a T239L60 NAVGEM configuration extending to ~0.005 hPa that allowed us to assimilate SSMIS UAS radiances using the CRTM forward operators in our 4D-Var solutions. Four separate experiments were performed during July 2010 that varied only in the types of mesospheric observations that were assimilated. Two experiments were, in essence, controls: a “NoMesoObs” experiment that assimilated no mesospheric observations at all, and another experiment that assimilated research-quality mesospheric temperatures from SABER and MLS. The other two experiments each assimilated UAS radiances: one that also assimilated MLS and SABER data and another that did not, so as to assess the mesospheric impacts of assimilating operationally available UAS data only.

Comparisons of results among the four experiments highlighted the large beneficial mesospheric impacts of assimilating SSMIS UAS radiances. Among the four experiments, the clear outlier was the NoMesoObs experiment, which produced, relative to the other three experiments, large zonal-mean temperature biases, much larger O-F standard deviations, and unrealistically strong zonal-mean mesospheric winds and Q2DW3 amplitudes. This occurred because of mesospheric biases in the model forecasts, which assimilated mesospheric observations substantially corrected in the other three experiments. In particular, the experiment that assimilated only UAS radiances produced results very similar to those assimilating MLS and SABER temperatures. An earlier NOGAPS-ALPHA 3D-Var production run assimilating mesospheric MLS and SABER temperatures had yielded large-scale mesospheric temperatures, winds and planetary-wave dynamics that were extensively validated in a number of previous studies (e.g., Hoppel et al. 2008; Eckermann et al. 2009; McCormack et al. 2010; Coy et al. 2011). Therefore, the close correspondence between mesospheric results

from the UAS-only and MLS+SABER experiments indicates that a reliable operational mesospheric analysis can be obtained by assimilating all the SSMIS UAS channels.

This is an important finding, since NWP systems are being developed to extend much higher, initially through the entire mesosphere (e.g., Eckermann et al. 2009) and eventually through the thermosphere (e.g., Wang et al. 2011). Yet, as our NoMesoObs experiment attests, operational versions of such systems must have real-time mesospheric observations to assimilate if they are to fully exploit their potential to forecast the mesosphere. Since SSMIS UAS channels provide our only source of real-time mesospheric observations for such systems at present, it is both reassuring and encouraging that our UAS-only experiments produce mesospheric analyses of comparable quality to those assimilating research-quality mesospheric temperature retrievals.

Looking further ahead, the picture is presently less encouraging. While there are two additional SSMIS instruments with UAS channels slated for future *F19* and *F20* deployments, there are currently no plans for UAS channels on any other meteorological satellite sensors, raising the possibility of a future mesospheric data void, despite having operational NWP systems extending through the MLT. This possibility will need to be addressed and remedied if future NWP systems are to fully exploit their potential for ground-to-space weather prediction.

Acknowledgments. This work was supported by the Office of Naval Research (ONR) through the Naval Research Laboratory's base 6.2 program (work unit: High-Altitude Data Assimilation for NWP) and ONR's Departmental Research Initiative on the Predictability of Seasonal and Intraseasonal Oscillations (Award N0001412WX21321). NAVGEM runs for this paper were made possible by a grant of computer time by the DoD High Performance Computing Modernization Program. We thank Gordon Wilson at AFRL for helpful discussions about DMSP and geomagnetic data.

REFERENCES

- Andrews, D. G., J. R. Holton, and C. B. Leovy, 1987: *Middle Atmosphere Dynamics*. Academic Press, 489 pp.
- Baldwin, M. P., D. W. J. Thompson, E. F. Shuckburgh, W. A. Norton, and N. P. Gillett, 2003: Weather from the stratosphere? *Science*, **301**, 317–318, doi:10.1126/science.1085688.
- Bell, W., and Coauthors, 2008: The assimilation of SSMIS radiances in numerical weather prediction models. *IEEE Trans. Geosci. Remote Sens.*, **46** (4), 886–900.
- Charlton, A. J., A. O'Neill, W. A. Lahoz, and A. C. Massacand, 2004: Sensitivity of tropospheric forecasts to stratospheric initial conditions. *Quart. J. Roy. Meteor. Soc.*, **130**, 1771–1792.
- Charney, J. G., and M. E. Stern, 1962: On the stability of internal baroclinic jets in a rotating atmosphere. *J. Atmos. Sci.*, **19**, 159–172.
- Clough, S. A., M. W. Shephard, E. J. Mlawer, J. S. Delamere, M. J. Iacono, K. Cady-Pereira, S.-A. Boukabara, and P. D. Brown, 2005: Atmospheric radiative transfer modeling: A summary of the AER codes. *J. Quant. Spectrosc. Radiat. Transfer*, **91**, 233–244.
- Coy, L., S. D. Eckermann, K. W. Hoppel, and F. Sassi, 2011: Mesospheric precursors to the major stratospheric sudden warming of 2009: Validation and dynamical attribution using a ground-to-edge-of-space data assimilation system. *J. Adv. Model. Earth Syst.*, **3**, M10002, doi:10.1029/2011MS000067.
- Dee, D., and A. M. daSilva, 1998: Data assimilation in the presence of forecast bias. *Quart. J. Roy. Meteor. Soc.*, **124**, 269–295.
- , and S. Uppala, 2009: Variational bias correction of satellite radiance data in the ERA-Interim reanalysis. *Quart. J. Roy. Meteor. Soc.*, **135**, 1830–1841.
- Dowdy, A. J., R. A. Vincent, D. J. Murphy, M. Tsutsumi, D. M. Riggan, and M. J. Jarvis, 2004: The large-scale dynamics of the mesosphere–lower thermosphere during the Southern Hemisphere stratospheric warming of 2002. *Geophys. Res. Lett.*, **31**, L14102, doi:10.1029/2004GL020282.
- Eckermann, S. D., 2009: Hybrid σ - p coordinate choices for a global model. *Mon. Wea. Rev.*, **137**, 224–245.
- , 2011: Explicitly stochastic parameterization of nonorographic gravity wave drag. *J. Atmos. Sci.*, **68**, 1749–1765.
- , and Coauthors, 2009: High-altitude data assimilation system experiments for the northern summer mesosphere season of 2007. *J. Atmos. Sol. Terr. Phys.*, **71**, 531–551.
- Garcia, R. R., D. R. Marsh, D. E. Kinnison, B. A. Boville, and F. Sassi, 2007: Simulation of secular trends in the middle atmosphere, 1950–2003. *J. Geophys. Res.*, **112**, D09301, doi:10.1029/2006JD007485.
- Garcia-Comas, M., and Coauthors, 2008: Errors in Sounding of the Atmosphere using Broadband Emission Radiometry (SABER) kinetic temperature caused by non-local-thermodynamic-equilibrium model parameters. *J. Geophys. Res.*, **113**, D24106, doi:10.1029/2008JD010105.
- Goncharenko, L. P., J. L. Chau, H.-L. Liu, and A. J. Coster, 2010: Unexpected connections between the stratosphere and ionosphere. *Geophys. Res. Lett.*, **37**, L10101, doi:10.1029/2010GL043125.
- Han, Y., F. Weng, Q. Liu, and P. van Delst, 2007: A fast radiative transfer model for SSMIS upper atmosphere sounding channels. *J. Geophys. Res.*, **112**, D11121, doi:10.1029/2006JD008208.
- , P. van Delst, and F. Weng, 2010: An improved fast radiative transfer model for special sensor microwave imager/sounder upper atmosphere sounding channels. *J. Geophys. Res.*, **115**, D15109, doi:10.1029/2010JD013878.
- Harris, B. A., and G. Kelly, 2001: A satellite radiance-bias correction scheme for data assimilation. *Quart. J. Roy. Meteor. Soc.*, **127**, 1453–1468.
- Hoppel, K., N. L. Baker, L. Coy, S. D. Eckermann, J. P. McCormack, G. E. Nedoluha, and D. E. Siskind, 2008: Assimilation of stratospheric and mesospheric temperatures from MLS and SABER into a global NWP model. *Atmos. Chem. Phys.*, **8**, 6103–6116, doi:10.5194/acp-8-6103-2008.
- Huang, F. T., H. G. Mayr, J. M. Russell, and M. G. Mlynczak, 2010: Ozone diurnal variations in the stratosphere and lower mesosphere, based on measurements from SABER on TIMED. *J. Geophys. Res.*, **115**, D24308, doi:10.1029/2010JD014484.

- Iacono, M. J., E. J. Mlawer, S. A. Clough, and J.-J. Morcrette, 2000: Impact of an improved longwave radiation model, RRTM, on the energy budget and thermodynamic properties of the NCAR community climate model, CCM3. *J. Geophys. Res.*, **105** (D11), 14873–14890.
- Ineson, S., and A. A. Scaife, 2009: The role of the stratosphere in the European climate response to El Niño. *Nat. Geosci.*, **2**, 32–36.
- Jung, T., and J. Barkmeijer, 2006: Sensitivity of tropospheric circulation to changes in the strength of the stratospheric polar vortex. *Mon. Wea. Rev.*, **134**, 2191–2207.
- Kunkee, D. B., G. A. Poe, D. J. Boucher, S. D. Swadley, Y. Hong, J. E. Wessel, and E. A. Uliana, 2008: Design and evaluation of the first special sensor microwave imager/sounder. *IEEE Trans. Geosci. Remote Sens.*, **46** (4), 863–883, doi:10.1109/TGRS.2008.917980.
- Kutepov, A. A., A. G. Feofilov, B. T. Marshall, L. L. Gordley, W. D. Pesnell, R. A. Goldberg, and J. M. Russell III, 2006: SABER temperature observations in the summer polar mesosphere and lower thermosphere: Importance of accounting for the CO₂ ν_2 quanta V–V exchange. *Geophys. Res. Lett.*, **33**, L21809, doi:10.1029/2006GL026591.
- Lambert, A., and Coauthors, 2012: Earth Observing System (EOS) Aura Microwave Limb Sounder (MLS) version 3.4 level-2 near-real-time data user guide. JPL D-48439_a, Jet Propulsion Laboratory, California Institute of Technology, Pasadena, CA, 13 pp. [Available online at <http://mls.jpl.nasa.gov/data/NRT-user-guide-v34.pdf>.]
- Livesey, N. J., and Coauthors, 2011: Earth Observing System (EOS) Aura Microwave Limb Sounder version 3.3 level 2 data quality and description document. JPL D-33509, Jet Propulsion Laboratory, California Institute of Technology, Pasadena, CA, 162 pp. [Available online at http://mls.jpl.nasa.gov/data/v3-3_data_quality_document.pdf.]
- Macmillan, S., and S. Maus, 2005: International geomagnetic reference field—The tenth generation. *Earth Planets Space*, **57**, 1135–1140.
- Manson, A., C. Meek, and X. Xu, 2010: Comment on “Global structure, seasonal and interannual variability of the migrating semidiurnal tide seen in the SABER/TIMED temperatures (2002–2007)” by Pancheva et al. (2009). *Ann. Geophys.*, **28**, 665–676.
- McCormack, J. P., S. D. Eckermann, K. W. Hoppel, and R. A. Vincent, 2010: Amplification of the quasi-two day wave through nonlinear interaction with the migrating diurnal tide. *Geophys. Res. Lett.*, **37**, L16810, doi:10.1029/2010GL043906.
- McLandress, C., 2002: The seasonal variation of the propagating diurnal tide in the mesosphere and lower thermosphere. Part II: The role of tidal heating and zonal mean winds. *J. Atmos. Sci.*, **59**, 907–922.
- Meek, C. E., A. H. Manson, and J. R. Drummond, 2011: Test of diurnal and semidiurnal tidal analysis of temperatures from SABER-like sampling of a realistic global model, CMAM-DAS. *Ann. Geophys.*, **29**, 723–730.
- Mlawer, E. J., S. J. Taubman, P. D. Brown, M. J. Iacono, and S. A. Clough, 1997: Radiative transfer for inhomogeneous atmospheres: RRTM, a validated correlated- k model for the longwave. *J. Geophys. Res.*, **102** (D14), 16663–16682.
- Mukhtarov, P., D. Pancheva, and B. Andonov, 2009: Global structure and seasonal and interannual variability of the migrating diurnal tide seen in the SABER/TIMED temperatures between 20 and 120 km. *J. Geophys. Res.*, **114**, A02309, doi:10.1029/2008JA013759.
- Nezlin, Y., Y. J. Rochon, and S. Polavarapu, 2009: Impact of tropospheric and stratospheric data assimilation on mesospheric prediction. *Tellus*, **61A**, 154–159, doi:10.1111/j.1600-0870.2008.00368.x.
- Norton, W. A., and J. Thuburn, 1999: Sensitivity of mesospheric mean flow, planetary waves, and tides to strength of gravity wave drag. *J. Geophys. Res.*, **104**, 30897–30911.
- Pancheva, D., P. Mukhtarov, and B. Andonov, 2009: Global structure, seasonal and interannual variability of the migrating semidiurnal tide seen in the SABER/TIMED temperatures (2002–2007). *Ann. Geophys.*, **27**, 687–703.
- Plumb, R. A., 1983: Baroclinic instability of the summer mesosphere: A mechanism for the quasi-two-day wave? *J. Atmos. Sci.*, **40**, 262–270.
- Polavarapu, S., S. Ren, Y. Rochon, D. Sankey, N. Ek, J. Koshyk, and D. Tarasick, 2005: Data assimilation with the Canadian Middle Atmosphere Model. *Atmos.–Ocean*, **43**, 77–100.
- Remsburg, E., and Coauthors, 2008: Assessment of the quality of the Version 1.07 temperature-versus-pressure profiles of the middle atmosphere from TIMED/SABER. *J. Geophys. Res.*, **113**, D17101, doi:10.1029/2008JD010013.
- , G. Lingenfelter, V. L. Harvey, W. Grose, J. Russell III, M. Mlynarczyk, L. Gordley, and B. T. Marshall, 2003: On the verification of the quality of SABER temperature, geopotential height, and wind fields by comparison with Met Office assimilated analyses. *J. Geophys. Res.*, **108**, 4628, doi:10.1029/2003JD003720.
- Ren, S., S. Polavarapu, S. R. Beagley, Y. Nezlin, and Y. J. Rochon, 2011: The impact of gravity wave drag on mesospheric analyses of the 2006 stratospheric major warming. *J. Geophys. Res.*, **116**, D19116, doi:10.1029/2011JD015943.
- Rienecker, M. M., and Coauthors, 2008: The GEOS-5 data assimilation system: Documentation of versions 5.0.1, 5.1.0, and 5.2.0. NASA Tech. Rep. 104606, Vol. 27, 118 pp.
- Riggin, D. M., C. K. Meyer, D. C. Fritts, M. J. Jarvis, Y. Murayama, W. Singer, R. A. Vincent, and D. J. Murphy, 2003: MF radar observations of seasonal variability of semidiurnal motions in the mesosphere at high northern and southern latitudes. *J. Atmos. Sol. Terr. Phys.*, **65**, 483–493.
- Roff, G., D. W. Thompson, and H. Hendon, 2011: Does increasing model stratospheric resolution improve extended-range forecast skill? *Geophys. Res. Lett.*, **38**, L05809, doi:10.1029/2010GL046515.
- Rosmond, T., and L. Xu, 2006: Development of NAVDAS-AR: Non-linear formulation and outer loop tests. *Tellus*, **58A**, 45–58.
- Sakazaki, T., M. Fujiwara, X. Zhang, M. E. Hagan, and J. M. Forbes, 2012: Diurnal tides from the troposphere to the lower mesosphere as deduced from TIMED/SABER satellite data and six global reanalysis data sets. *J. Geophys. Res.*, **117**, D13108, doi:10.1029/2011JD017117.
- Sankey, D., S. Ren, S. Polavarapu, Y. J. Rochon, Y. Nezlin, and S. Beagley, 2007: Impact of data assimilation filtering methods on the mesosphere. *J. Geophys. Res.*, **112**, D24104, doi:10.1029/2007JD008885.
- Schwartz, M. J., and Coauthors, 2008: Validation of the Aura Microwave Limb Sounder temperature and geopotential height measurements. *J. Geophys. Res.*, **113**, D15S11, doi:10.1029/2007JD008783.
- Stogryn, A., 1989: Mesospheric temperature sounding with microwave radiometers. *IEEE Trans. Geosci. Remote Sens.*, **27** (3), 332–338.
- Swadley, S., G. Poe, W. Bell, Y. Hong, D. B. Kunkee, I. S. McDermid, and T. Leblanc, 2008: Analysis and characterization of the SSMIS Upper Atmosphere Sounding Channel

- Measurements. *IEEE Trans. Geosci. Remote Sens.*, **46** (4), 962–983, doi:10.1109/TGRS.2008.916980.
- , —, N. Baker, B. Ruston, W. Bell, D. Kunkee, and D. Boucher, 2010: SSMIS radiance assimilation, calibration anomaly mitigation and assimilation results from F18. *Proc. 17th Int. TOVS Study Conf.*, Monterey, CA, International TOVS Working Group, ITSC-17.
- Thompson, D. W. J., M. P. Baldwin, and J. M. Wallace, 2002: Stratospheric connection to Northern Hemisphere wintertime weather: Implications for prediction. *J. Climate*, **15**, 1421–1428.
- Wang, H., T. J. Fuller-Rowell, R. A. Akmaev, M. Hu, D. T. Kleist, and M. D. Iredell, 2011: First simulations with a whole atmosphere data assimilation and forecast system: The January 2009 major sudden stratospheric warming. *J. Geophys. Res.*, **116**, A12321, doi:10.1029/2011JA017081.
- Watanabe, S., and S. Miyahara, 2009: Quantification of the gravity wave forcing of the migrating diurnal tide in a gravity wave-resolving general circulation model. *J. Geophys. Res.*, **114**, D07110, doi:10.1029/2008JD011218.
- Waters, J. W., and Coauthors, 2006: The Earth Observing System Microwave Limb Sounder (EOS MLS) on the Aura satellite. *IEEE Trans. Geosci. Remote Sens.*, **44**, 1075–1092.
- Xu, L., T. Rosmond, and R. Daley, 2005: Development of NAVDAS-AR: Formulation and initial tests of the linear problem. *Tellus*, **57A**, 546–559.
- Xu, X., A. H. Manson, C. E. Meek, C. Jacobi, C. M. Hall, and J. R. Drummond, 2011: Mesospheric wind semidiurnal tides within the Canadian Middle Atmosphere Model Data Assimilation System. *J. Geophys. Res.*, **116**, D17102, doi:10.1029/2011JD015966.
- , —, —, D. M. Riggan, C. Jacobi, and J. R. Drummond, 2012: Mesospheric wind diurnal tides within the Canadian Middle Atmosphere Model Data Assimilation System. *J. Atmos. Sol. Terr. Phys.*, **74**, 24–43.
- Zhang, X., J. M. Forbes, M. E. Hagan, J. M. Russell III, S. E. Palo, C. J. Mertens, and M. G. Mlynczak, 2006: Monthly tidal temperatures 20–120 km from TIMED/SABER. *J. Geophys. Res.*, **111**, A10S08, doi:10.1029/2005JA011504.